

# Cavity-enhanced narrowband spectral filters using rare-earth ions doped in thin-film lithium niobate

Yuqi Zhao<sup>1,2\*</sup>, Dylan Renaud<sup>3</sup>, Demitry Farfurnik<sup>4</sup>, Subhojit Dutta<sup>1,2</sup>, Neil Sinclair<sup>3\*</sup>,  
Marko Lončar<sup>3</sup>, Edo Waks<sup>1,2\*</sup>

<sup>1</sup>*Department of Electrical and Computer Engineering, University of Maryland, College Park, MD, 20742, USA*

<sup>2</sup>*Institute for Research in Electronics and Applied Physics (IREAP), University of Maryland, College Park, MD, 20742, USA*

<sup>3</sup>*John A. Paulson School of Engineering and Applied Sciences, Harvard University, 29 Oxford Street, Cambridge, MA, 02138, USA*

<sup>4</sup>*Department of Electrical and Computer Engineering, North Carolina State University, Raleigh, NC, 27606, USA*  
*\* yuq1zhao@umd.edu, neils@seas.harvard.edu, edowaks@umd.edu*

**key words:** on-chip, thin-film lithium niobate, rare-earth ions, cavity, optical filtering, ring resonator

## Abstract:

On-chip optical filters are fundamental components in optical signal processing. While rare-earth ion-doped crystals offer ultra-narrow optical filtering via spectral hole burning, their applications have primarily been limited to those using bulk crystals, restricting their utility. In this work, we demonstrate cavity-enhanced spectral filtering based on rare-earth ions in an integrated nonlinear optical platform. We incorporate rare-earth ions into high quality-factor ring resonators patterned in thin-film lithium niobate. By spectral hole burning in a critically-coupled resonance mode, we achieve bandpass filters ranging from 7 MHz linewidth, with 13.0 dB of extinction, to 24 MHz linewidth, with 20.4 dB of extinction. These filters outperform those of the highest quality factor ring resonators demonstrated in the thin-film lithium niobate integrated platform. Moreover, the cavity enables reconfigurable filtering by varying the cavity coupling rate. For instance, as opposed to the bandpass filter, we demonstrate a bandstop filter utilizing an under-coupled ring resonator. Such versatile integrated spectral filters with high extinction ratio and narrow linewidth could serve as fundamental components for optical signal processing and optical memories on-a-chip.

On-chip optical filters are a fundamental building block in optical computing<sup>1</sup>, optical spectrometry<sup>2</sup>, sensing<sup>3</sup>, microwave photonics<sup>4</sup>, ultrafast pulse shaping<sup>5-7</sup>, and wavelength division multiplexing<sup>8</sup>. Integrated optical filters that can simultaneously achieve narrow bandwidth, low loss, and high extinction ratios are lacking, particularly for filter bandwidths below tens of MHz<sup>9</sup>. Rare-earth-ion-doped crystals can realize ultra-narrow optical filters via spectral hole burning<sup>9</sup>. In this approach, a narrowband laser excites the ions to remove a narrow absorption line from the inhomogeneously broadened absorption spectrum of the ions, resulting in a bandpass filter at the targeted wavelength. The resulting linewidth could approach two times the ion homogeneous linewidth, which could be very narrow, e.g., 146 Hz in Er:YSO<sup>10</sup>. However, such optical filters have primarily been studied in bulk crystals, with motivation primarily for

ultrasound detection<sup>11–13</sup>. While rare-earth-ion-doped nanophotonics have been extensively explored for quantum memory<sup>14–16</sup>, single ion qubit<sup>17</sup>, and cavity quantum emitters<sup>18</sup>, on-chip optical filtering and signal processing using rare-earth ions has not been thoroughly investigated.

Thin-film lithium niobate has emerged as a promising integrated host platform for rare-earth ions. Furthermore, this material has underpinned a range of high-performance integrated nanophotonic components<sup>19</sup> due to its exceptional electro-optic and nonlinear properties<sup>20</sup>. Rare-earth ion based amplifiers<sup>21,22</sup>, lasers<sup>23</sup>, as well as quantum memories<sup>16</sup> have been demonstrated in thin-film lithium niobate. The ultra-low propagation loss (3 and 6 dB/m at 1550 nm<sup>24,25</sup> and 638 nm<sup>26</sup> respectively) in this platform has also enabled high quality factor photonic cavities, which has already achieved Purcell enhancement of single ion emission<sup>27</sup> and long range cooperative resonances<sup>18</sup>. These distinctive properties make rare-earth ion-doped thin-film lithium niobate an ideal material to implement on-chip optical filters utilizing photonic cavities.

In this work, we demonstrate cavity-enhanced spectral filtering based on rare-earth ion-doped thin-film lithium niobate. We incorporate thulium ( $\text{Tm}^{3+}$ ) ions into high-quality factor X-cut ring resonators patterned in thin-film lithium niobate. This cut is chosen as it is the same as that primarily used for thin-film lithium niobate modulators<sup>28</sup>. Due to the low propagation loss in the cavity, we attain a ring resonator structure with loss dominated by rare-earth ion absorption. By spectral hole burning at the resonance frequency of a critically-coupled mode of the resonator, in which all light is absorbed by thulium ions, we attain narrowband filters with linewidths ranging from 7 MHz with 13.0 dB of extinction, to 24 MHz with 20.4 dB of extinction. The 24 MHz-linewidth filter has an extinction ratio 70 times greater than that of a conventional waveguide of identical length. Cavity coupling also enables creation of filter functions that are unattainable using waveguides. For example, using an under-coupled cavity we show a bandstop filter as opposed to a bandpass filter. Such narrowband, high extinction ratio integrated spectral filters could serve as fundamental components for optical signal processing and optical memories on-a-chip.

Thulium ions doped in lithium niobate exhibit a quasi-three level energy structure, as shown in Fig. 1A. This configuration includes a ground level  $^3H_6$ , an excited level  $^3H_4$ , and an intermediate level  $^3F_4$ . The transition between the lowest energy level in  $^3H_4$  multiplet and the ground level  $^3H_6$  features a resonance wavelength of  $\sim 794$  nm. Known for its strong absorption<sup>29</sup> and long coherence time of  $1.4 \mu\text{s}$  at a temperature of  $4\text{K}$ <sup>16</sup>, this transition is extensively studied for spectral hole burning and quantum information applications. In this work, we utilize the 794 nm optical transition inhomogeneously broadened by an ensemble of thulium ions to burn spectral holes by optically pumping the ground level population to the  $^3H_4$  level. Such spectral holes have a decay rate determined by the lifetimes of both the  $^3H_4$  level ( $162 \pm 16 \mu\text{s}$ ) and the  $^3F_4$  level ( $3 \pm 1.6 \text{ms}$ )<sup>30</sup>.

Fig. 1B shows a schematic of the proposed design of the cavity-enhanced spectral filter based on a ring resonator. The ring resonator consists of a closely spaced ring and a bus waveguide patterned in thin-film lithium niobate doped with  $\text{Tm}^{3+}$  ions at a density of 0.1%. Light is coupled in and out of the resonator through grating couplers at both ends of the bus waveguide. Part of

this light is coupled to the ring, as quantified by the coupling rate  $\kappa_e$ , which is determined by the gap between the bus and ring waveguides. As the light propagates around the ring resonator, the ring loss rate  $\kappa_{in} = \kappa_{ion} + \kappa_p$  describes how fast the light is attenuated due to the dominant  $\text{Tm}^{3+}$  ion absorption ( $\kappa_{ion}$ ) and an additional low propagation loss ( $\kappa_p$ ), where  $\kappa_{ion} \gg \kappa_p$ .

A critical coupling condition is achieved when  $\kappa_e = \kappa_{in}$ , in which all the light is coupled from the bus waveguide to the ring and lost during propagation, resulting in zero transmission to the output grating coupler. We achieve a cavity-enhanced bandpass filter by utilizing a resonance mode (at  $\sim 794$  nm wavelength) that is initially critically-coupled and burning a spectral hole at the center of the mode so that  $\kappa_{ion} = 0$  and  $\kappa_e \gg \kappa_{in}$ , resulting in high transmission at the burning wavelength. Meanwhile, the remaining incident light displays zero transmission, leading to a high extinction ratio for the bandpass filter. In contrast, for a conventional waveguide of the same length, absorption by the thulium ions is limited by the length of the device, which leads to a low extinction ratio (Fig. 1C). Although increasing the waveguide length or the ion doping concentration could enhance the ion absorption and improve the extinction ratio, a waveguide with high optical depth could experience higher power broadening in the front than the back. Moreover, a longer waveguide requires a larger device footprint, which is unfavorable for on-chip integration.

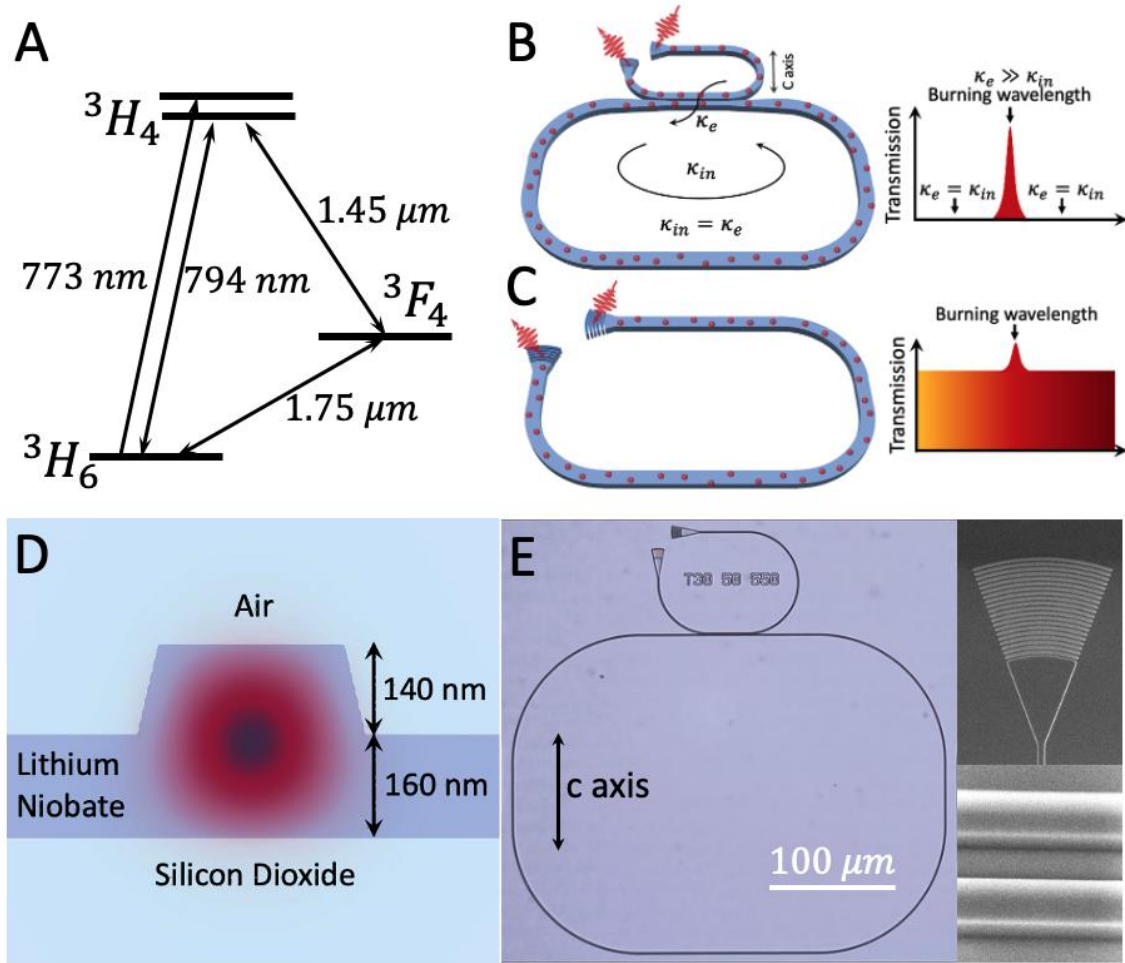


**Fig. 1** (A) A simplified energy level structure and approximate transition wavelengths of  $\text{Tm}^{3+}$  ions in thin-film lithium niobate. (B) Schematic of the proposed cavity-enhanced spectral filter design based on a critically-coupled ring resonator. By spectral hole burning at the target wavelength, the initial critically-coupled condition can be changed into strongly over-coupled condition ( $\kappa_e \gg \kappa_{in} = \kappa_p$ ) at the burning wavelength, which gives high transmission. Meanwhile, the light at the unburned wavelength remains zero transmission, which enables a high extinction ratio bandpass filter. (C) Schematic of a bandpass filter based on a conventional waveguide of the same length of the ring. Due to the small absorption limited by the length of the waveguide, the filter features a low extinction ratio. (D) Schematic of the rib waveguide design cross section and the simulated fundamental TE mode inside the waveguide. (E) An optical microscope image of a representative fabricated ring resonator and scanning electron microscopy images of its coupling region and grating coupler. The long coupling region allows reaching high coupling rates  $\sim 50$  GHz at 794 nm wavelength.

We first design the geometry of the thin-film lithium niobate ring and bus waveguides to maintain single transverse mode light operation with minimal propagation loss. For both waveguides, we use a rib design consisting of a strip on a slab structure, as shown in Fig. 1D. We choose the height of the strip and slab to be 140 and 160 nm, respectively. The sidewall angle is assumed to be  $62^\circ$  with respect to the horizontal direction, based on a previously reported fabrication approach<sup>26,28</sup>. A narrow width waveguide is beneficial for single mode light operation (i.e., the fundamental transverse electric (TE) mode) and strong interaction with ions. However, a larger width helps decrease the propagation loss by reducing the overlap between the optical mode and the

waveguide sidewall. As propagation loss in the bus waveguide does not affect the total loss rate ( $\kappa_{in}$ ) in the ring, we set the width to be 450 nm, with a bending radius of 40  $\mu m$ , which supports only the fundamental TE mode at the target wavelength of 794 nm, according to finite difference time domain (FDTD) simulations<sup>31</sup>. However, for the ring waveguide, both single mode operation and minimal propagation loss are desired. Considering this trade-off, we use a ring design that tapers from a 650 nm wide waveguide down to a narrower width of 450 nm in the coupling region, which we set to be 30  $\mu m$  long. FDTD simulations of this coupling region verify that single mode coupling occurs at 794 nm. We also choose a large bending radius of 100  $\mu m$  for the ring waveguide to minimize the bending loss, which is  $4 \times 10^{-6}$  dB/m according to simulations. Based on these parameters, the lengths of the bus and ring waveguides are 188  $\mu m$  and 1000  $\mu m$ , respectively.

We then determine the coupling gap between the bus and ring waveguides to achieve the desired initial critical coupling condition ( $\kappa_e = \kappa_{in}$ ). In addition to the length of the ring (1000  $\mu m$ ),  $\kappa_{in}$  is determined by the configuration of the lithium niobate chip. We choose an X-cut configuration as it features anisotropic in-plane ion absorption with respect to the optical axis (c-axis) in addition for its use for modulators. As a result, we achieve low-loss coupling by aligning the straight coupling regions of the waveguides perpendicular to the c-axis<sup>30,32,33</sup>, enabling simpler operation and analysis (see Fig. 1B). Based on this alignment, we estimate  $\kappa_{in}$  to be 51.1 GHz by calculating the ion absorption at 794 nm in one round trip through the ring waveguide, which is given by the product of the ion absorption coefficient (3.5 dB/mm)<sup>30</sup> and the length of the ring that overlaps with the c-axis (500  $\mu m$ ). Then, to determine the coupling gap value that enables  $\kappa_e = \kappa_{in}$ , we simulate the coupling rate ( $\kappa_e$ ) of the 30  $\mu m$  long coupling region of the bus and ring waveguides as a function of the gap distance. Our simulations show a gap of 510 nm between the bus and ring waveguides should result in the critical coupling condition (see Supplemental Information Section 1).

We then fabricate the proposed device design using electron beam lithography and dry etching. The chip is composed of a 300 nm thin film lithium niobate wafer doped with 0.1%  $Tm^{3+}$  ions over a 2-  $\mu m$  -thick silicon dioxide layer grown on an undoped bulk silicon substrate. Using electron beam lithography, we patterned the proposed ring resonator design into the lithium niobate chip, and then removed 140 nm of the unpatterned region using inductively coupled reactive ion etching with  $Ar^+$  plasma (ICP-RIE) (see Methods). Given our simulations, we fabricated multiple ring resonators with coupling gaps that ranged from 410 nm to 610 nm at 5 nm steps. This wide range allows us to investigate the critical coupling condition within fabrication intolerance, as well as explore cavity-enhanced filters that feature other initial coupling conditions (e.g.,  $\kappa_e < \kappa_{in}$ ,  $\kappa_e > \kappa_{in}$ ). Fig. 1e shows an optical microscopy image of a representative ring resonator and scanning electron microscopy images of its coupling region and grating coupler. For comparison, we also fabricated conventional waveguides of 650 nm in width and 1000  $\mu m$  in length on the same lithium niobate chip.

The propagation loss of both the fabricated ring and conventional waveguide is estimated to be around 0.7 dB/cm at 794 nm. This value is obtained from a nearly critically-coupled bare ring resonator with an identical ring waveguide design, fabricated using the same methods on a

separate undoped thin-film lithium niobate chip. The low propagation loss results in a high quality factor of the bare ring resonator, measured to be  $Q_L = 5.42 \times 10^5$ , corresponding to an intrinsic quality factor of  $Q_I = 1.1 \times 10^6$  at 794 nm (see Supplemental Information Section 2).

We first characterize the ring resonance modes using photoluminescence. When excited to the fifth level of the  $^3H_4$  excited level multiplet<sup>33</sup> by a continuous wave (CW) laser at  $\sim 773$  nm, the thulium ions decay to the  $^3H_6$  level and photoluminescence at 794 nm (Fig. 1A). Using a ring resonator with a coupling gap of 550 nm, we measure the photoluminescence spectra of the  $Tm^{3+}$  ions at 4 K at different excitation wavelengths between 773 and 774 nm. Figure 2A shows the photoluminescence emission of the device at excitations of 773.39 nm and 773.53 nm. For 773.39 nm excitation, narrow-linewidth photoluminescence peaks appear in the spectrum, which we attribute to the resonances of the ring resonator. Background photoluminescence emission appears in the spectrum taken at 773.53 nm excitation, which is off-resonant to the cavity. The resonance peaks are equally distributed with a free spectral range (FSR) of 0.263 nm. This value is consistent with the predicted free spectral range for the fundamental TE mode, given by  $FSR = \lambda^2/n_g L = 0.268$  nm, where  $\lambda$  and  $L$  represent the wavelength and total length of the ring waveguide, respectively, and  $n_g$  is the simulated TE mode group index ( $n_g = 2.33$ ). We therefore attribute the observed resonance peaks to the fundamental TE modes of the ring waveguide.

We next measure the transmission spectrum of the device. To avoid affecting the ion absorption by hole burning, we use a weak superluminescence diode (SLD) source (10 nW), with a center wavelength of 810 nm and a bandwidth of 30 nm. Figure 2B shows the measured transmission spectrum for the same device used in panel A. The device exhibits a series of spectral dips whose free spectral range (0.263 nm) is consistent with that of the photoluminescence spectrum. Within the wavelength range of the thulium ion absorption (orange line in Fig. 2B), we observe deep spectral dips. The transmission spectrum of the dips at wavelengths that correspond to the maximum absorption of the ions drop to nearly zero, suggesting that we are close to critical coupling ( $\kappa_e = \kappa_{in}$ ). The contrast of the dips outside the absorption range of the thulium ions is very small, indicating that these modes are over-coupled ( $\kappa_e \gg \kappa_{in} = \kappa_p$ ).

To further confirm whether the critical coupling condition is met and determine the exact values of  $\kappa_e$  and  $\kappa_{in}$ , we conduct a higher resolution transmission measurement using a narrowband tunable laser. We focus on the resonance mode at 794.535 nm, as indicated by the blue arrow in Fig. 2B. We scan the wavelength of an attenuated tunable CW laser (resolution 0.001 nm) and measure the power of the transmitted light as a function of the wavelength, as shown in Fig. 2C. We fit the resulting transmission spectrum of the 794.535 nm resonance mode to the all-pass ring resonator transmission equation<sup>34</sup> (blue line, Fig. 2C):

$$T = \frac{r^2 + a^2 - 2ar\cos\varphi}{1 + r^2a^2 - 2ar\cos\varphi} \quad (1)$$

where  $r$  is the amplitude coefficient of light that remains propagating along the bus waveguide at the coupling region,  $a$  is the amplitude attenuation factor in the ring waveguide, and  $\varphi$  is the

round-trip phase given by  $2\pi L/\lambda$ . The transmission at the fitted resonance dip is  $T = 1\%$  of the light coupled into the bus waveguide, which is close to zero transmission for the ideal critical coupling condition. From the fit, we determine the fitting parameters to be  $r = 0.83$  and  $a = 0.80$ . Using these values, we calculate  $\kappa_e$  and  $\kappa_{in}$  as 46.7 GHz and 54.7 GHz via their relations<sup>35</sup>:

$$\kappa_e = \frac{2c \cdot \cos^{-1}\left(\frac{2r}{1+r^2}\right)}{n_g L} \quad (1)$$

$$\kappa_{in} = \frac{2c \cdot \cos^{-1}\left(\frac{2a}{1+a^2}\right)}{n_g L} \quad (2)$$

where  $c$  is the vacuum light speed and  $n_g$  is the group index of the TE mode. The extracted ring loss rate is also comparable to the predicted  $\kappa_{in}$  value (52.9 GHz) that we estimate from the measured propagation loss (0.7 dB/cm) and ion absorption (3.5 dB/mm at 794.535 nm, see orange line in Fig. 2B). Based on these results, we conclude that a near critical coupling condition is successfully achieved for this resonance mode at 794.535 nm in a ring resonator with a coupling gap of 550 nm, which is close to the value predicted by simulations.

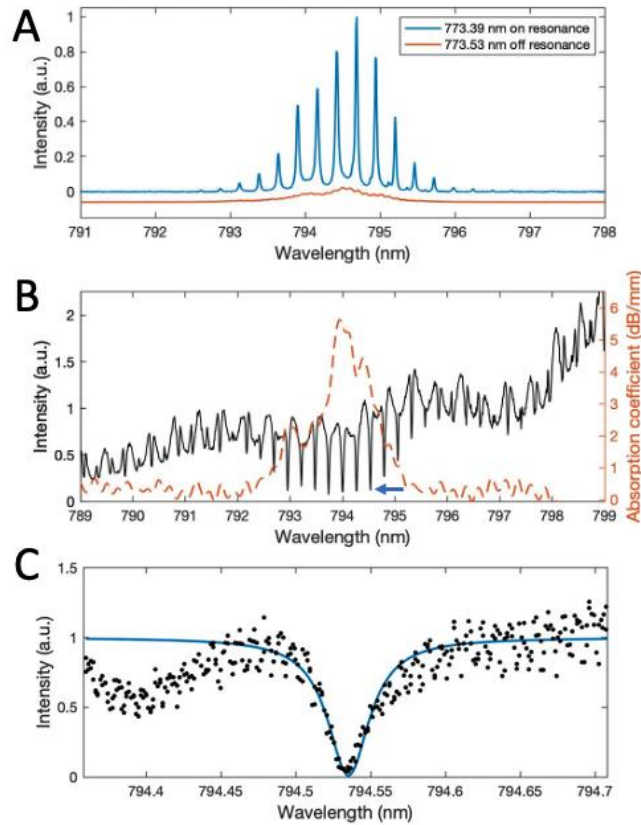


**Fig 2.** (A) The photoluminescence spectrum of a ring resonator with a 550 nm coupling gap, excited by light that is on-resonant (773.39 nm, blue) and off-resonant (773.53 nm) to the ring. The spectrum is normalized to the maximum photoluminescence intensity. (B) The transmission spectrum of the same ring resonator (black), normalized to the

intensity of non-resonant wavelength at  $\sim 794$  nm. The overall shape of the spectrum is due to the profile of the SLD source we used. The absorption spectrum of the  $Tm^{3+}$  ions measured from a conventional waveguide (orange) is also shown for comparison. (C) The transmission spectrum of the resonance mode at 794.535 nm (blue arrow in (B)), fitted with a Lorentzian curve and normalized to the fitted constant background intensity. The small resonance at 794.4 nm is due to Fabry-Perot interference between optics in the measured setup.

To create a cavity-enhanced bandpass filter, we burn a deep spectral hole in the critically-coupled resonance mode at 794.535 nm. We generate a pulse of 50  $\mu s$  duration to excite the ions from the  $^3H_6$  ground level to the  $^3H_4$  excited level, followed by two weak probe pulses to investigate the transmission spectrum of the resulting spectral hole (see Methods). To maximize the extinction ratio of the filter, we use a burning power of 250 nW to remove all ion absorption at the target wavelength and burn the deepest possible hole. The frequency of the probe light is swept through a 100 MHz bandwidth around the burning frequency and the transmitted light is measured as a function of frequency to obtain the transmission spectrum of the filter.

Fig. 3A shows the measured relative transmission spectrum of the device (blue line), which we define as the transmission spectrum  $T(\omega)$  normalized to the minimum background transmission  $T_{back}$  measured without any burned spectral hole. This spectrum features a strong transmission peak at the burning wavelength, with the corresponding extinction ratio given by the maximum value at the peak. By fitting the data with a Lorentzian function, we extract a narrow linewidth of  $24 \pm 0.9$  MHz and a high extinction ratio of  $110 \pm 1.1$  (20.4 dB). These results demonstrate that after spectral hole burning the ring resonator functions as a narrow bandpass filter for the targeted wavelength.

For comparison, we also create a bandpass filter by spectral hole burning a conventional lithium niobate waveguide of the same length as the ring resonator (1000  $\mu m$ ). To remove all ion absorption at the target wavelength, we use a burning power that is 10-times as strong as the power used in the ring resonator (2500 nW) to compensate for the  $\sim 10$ -times power enhancement in the ring waveguide due to resonance<sup>36</sup> (see Supplemental Information Section 3). The orange line in Fig. 3A shows the relative transmission spectrum of the waveguide, which features a linewidth of  $18 \pm 0.7$  MHz and a low extinction ratio of  $1.52 \pm 0.01$ . The theoretical maximum extinction ratio is determined by the optical depth (OD) of the device, which we can calculate from the product of the ion absorption coefficient (Fig. 2B) and the length of overlap of the waveguide with the c-axis of the lithium niobate chip (500  $\mu m$ ). From these values, we find  $OD = 0.43$ , which gives a theoretical maximum extinction ratio of  $e^{OD} = e^{0.43} = 1.54$ . Therefore, the measured extinction ratio (1.52) of the conventional waveguide is already near the maximum and cannot be further improved, even using a higher burning power. In comparison, the cavity-enhanced bandpass filter features a 70-times higher extinction ratio while maintaining the same device footprint.

We also investigate the dependence of the extinction ratio of the cavity-enhanced filter on the hole burning power. We use the same conditions for the spectral hole burning experiment, fixing the burning pulse duration to be 50  $\mu s$  while changing the burning power. Figure 3B shows the measured power-dependent extinction ratio of spectral holes burned in the same critically-coupled resonance mode in the 550 nm gap ring resonator (black), which we compared to a 2000



$\mu\text{m}$  conventional waveguide (blue). The extinction ratio of the spectral hole increases with the burning power in both cases, as more ions are excited at a higher power until the deepest hole is created. For the cavity-enhanced filter, the hole extinction ratio grows from 20 to 110 as the power increases from 30 nW to 250 nW, while for the case of the conventional waveguide, the extinction ratio increases from 2.3 and gradually saturates at 3.2 for a power of 100 nW to 2300 nW. These results show that the critically-coupled resonance mode greatly enhances the extinction ratio of the cavity-enhanced filter. Even at the smallest investigated burning power (30 nW), the cavity-enhanced filter features a 6-times higher extinction ratio compared to the maximum of the conventional waveguide. We would expect to see a saturation trend for the cavity-enhanced filter at higher burning powers. However, in our current setup, the resonance modes in the ring resonator exhibit thermo-optic shifts at high power<sup>37</sup>. As a result, we were not able to increase the burning power over 250 nW without losing the initial critical-coupling condition. Nevertheless, it is worth noting that a higher power and further improvement on extinction ratio is possible by compensating this red shift using DC tuning<sup>38</sup>.

We also explore the power-dependent linewidths of both the cavity-enhanced filter and waveguide filter. Figure 3C shows the linewidths of the same spectral holes investigated in Fig. 3B, at different burning powers in both the ring resonator (black) and a 2000  $\mu\text{m}$  waveguide (blue). In Fig. 3C, the hole linewidth increases at higher burning powers for both the ring resonator and waveguide, which can be explained by the power-broadening effect of the spectral hole<sup>39,40</sup>. The linewidth of the cavity-enhanced filter increases from 7 MHz to 24 MHz as the power increases from 30 nW to 250 nW, while the linewidth of the conventional waveguide filter grows from 5 MHz to 17 MHz at powers from 100 nW to 2300 nW, which can be fitted to the broadening model described in [40] (see Supplemental Information Section 4). The minimum achievable linewidth is extracted to be 2.3 MHz from the zero-excitation intercept of the fitted curve, which is limited by both the homogeneous linewidth and the laser linewidth (see Supplemental Information Section 4). For the same burning power, the cavity-enhanced filter features a linewidth that is approximately three times as broad as that of the conventional waveguide, which we attribute to the enhanced burning power via the ring resonance. Thus, although the filter bandwidth of the cavity is slightly degraded relative to a waveguide, the linewidth broadening is small compared to the significant improvement in the extinction ratio. By utilizing different burning powers, this tradeoff between the filter extinction ratio and linewidth can be managed for different applications.

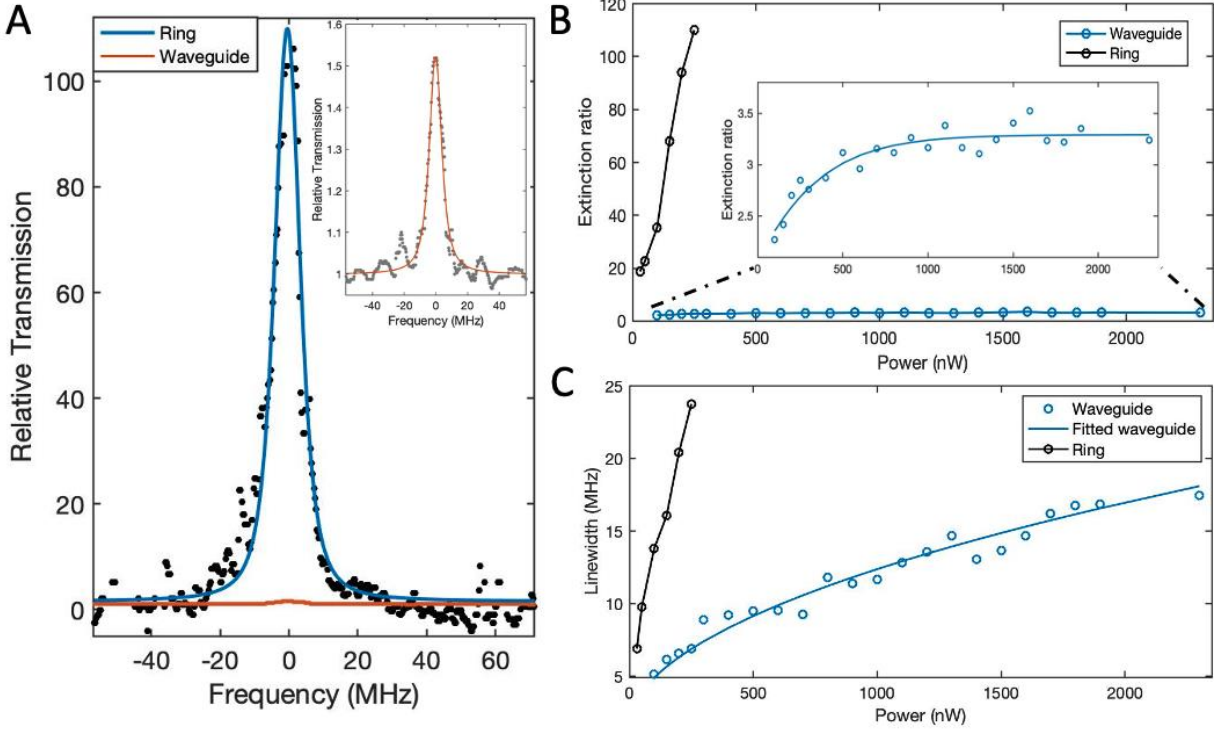
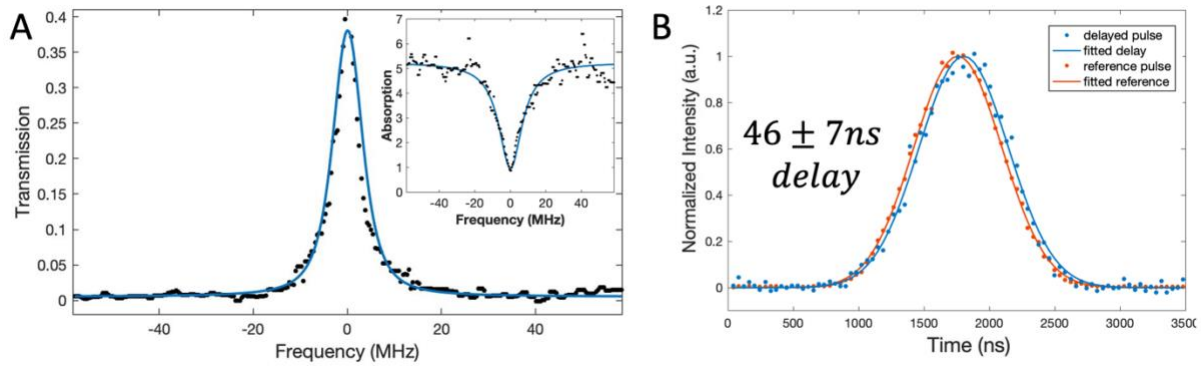


**Fig. 3** (A) The relative transmission spectra of a deep spectral hole burned with 250 nW burning power in the critically-coupled resonance mode in a 550 nm gap ring resonator (blue), and a spectral hole burned with 2500 nW burning power in a 1000  $\mu\text{m}$  conventional waveguide (orange and inset). Both spectra are normalized to the minimum background transmitted power. (B) The extinction ratio of the cavity-enhanced (black) and conventional waveguide filters (blue), as a function of the burning power. Note, for this measurement we use a longer conventional waveguide (2000  $\mu\text{m}$ ) to achieve a higher maximum extinction ratio compared to in Fig. 3A (orange) to better observe the trend of the extinction ratio as a function of the burning power. (C) The linewidth of the cavity-enhanced filter (black) and the conventional waveguide filter (blue, 2000  $\mu\text{m}$  in length), as a function of the burning power.

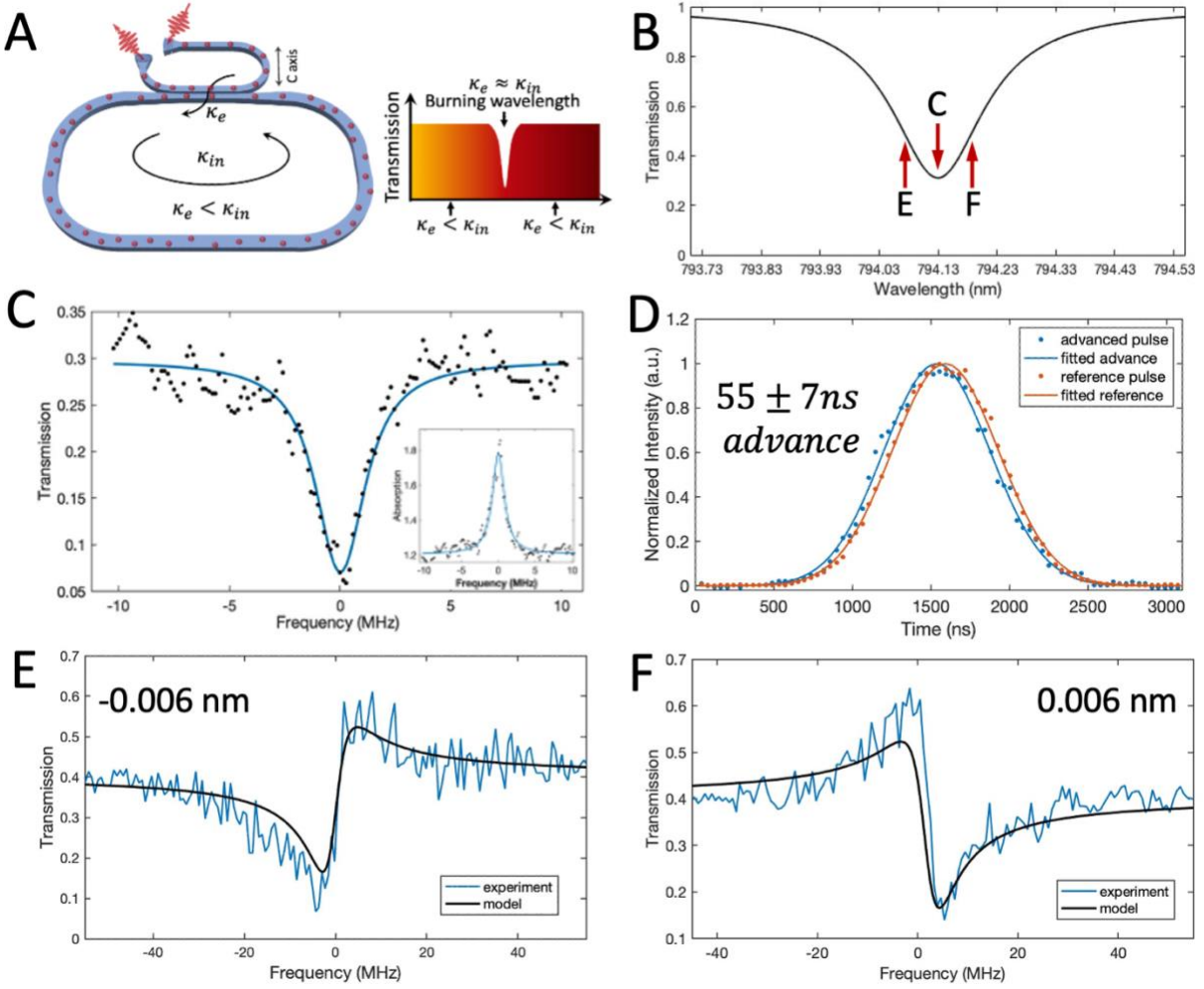
Apart from the frequency filtration effect, a bandpass filter also imparts a group delay on an incident light pulse due to dispersion<sup>41</sup>. To demonstrate this time domain response of the cavity-enhanced bandpass filter, we first burn a spectral hole in the critically-coupled resonance mode and then send a weak Gaussian-shaped probe signal of duration 1  $\mu\text{s}$  with the same carrier frequency through the hole (see Methods). For the spectral hole burning, we use a burning power of 150 nW, which gives a good balance in the resulting extinction ratio (70) and hole linewidth (16 MHz). Figure 4A shows the transmission spectrum of the burned spectral hole, and its absorption spectrum, calculated by  $\alpha(\omega) = -\ln [T(\omega)]$  (inset). The spectral hole features a linewidth of  $\Delta = 16 \text{ MHz}$  and a hole depth of  $d = 4.25$ .

Figure 4B shows the measured arrival time of the probe pulse transmitted through the burned spectral hole. For comparison, we also measure the arrival time of a reference probe pulse transmitted through a very broad spectral hole (>1 GHz) burned with 80  $\mu\text{W}$  power, which is considered to have negligible group delay (orange, see Methods). By fitting both pulses with Gaussian functions, we extract the delay of the probe pulse center to be  $46 \pm 7 \text{ ns}$ , which is

consistent with the theoretical delay predicted from the hole depth  $d$  and linewidth  $\Delta$  as:  $\Delta t = d/2\pi\Delta = 42 \text{ ns}$ <sup>37</sup>. This consistency between the measured time response of the cavity-enhanced filter with the predicted time delay further validates its properties as a bandpass filter.



**Fig. 4** (A) The transmission and absorption (inset) spectra of a spectral hole burned with 150 nW burning power in a critically-coupled resonance mode of the ring resonator. (B) The arrival time of a Gaussian-shaped weak probe pulse transmitted through the burned spectral hole shown in (A) (blue) is delayed by  $46 \pm 7 \text{ ns}$ , as compared to a reference probe pulse (orange).



**Fig. 5** (A) A schematic of a bandstop filter created by burning a spectral hole in an initially under-coupled resonance mode. (B) The calculated transmission spectrum of an under-coupled resonance mode. (C) The transmission spectrum of a bandstop filter created by burning a spectral hole at the center of the resonance mode. (D) The arrival time of a probe pulse transmitted through the bandstop filter in (C) (blue), as well as an unshifted reference probe pulse (orange). (E, F) The transmission spectra of a Fano-shaped bandstop filter created by burning a spectral hole at a wavelength that is detuned from the resonance by (E)  $-0.006$  nm and (F)  $0.006$  nm.

A distinctive advantage of using cavity-coupled emitters is the ability to produce reconfigurable filtering behavior by controlling the cavity coupling rate. As an example, in contrast to the bandpass filter, we demonstrate a method to generate a bandstop filter (Fig. 5A). To achieve this type of filter, we employ a resonance mode that is initially in an under-coupled condition ( $\kappa_e < \kappa_{in}$ ) with  $r > a$  according to Eq. (2-3). Under this condition, the resonance wavelength exhibits a large transmission, as described by substituting  $\varphi = 0$  in Eq. (1):

$$T = \frac{(r - a)^2}{(1 - ra)^2} \quad (3)$$

By burning a spectral hole in the resonance mode, we could decrease  $\kappa_{ion}$ , reaching the critical coupling condition  $\kappa_e \approx \kappa_{in} = \kappa_{ion} + \kappa_p$  at the burning wavelength, resulting in  $r = a$  and zero transmission in Eq. (4). This reduced transmission at the burning wavelength enables a bandstop filter.

To demonstrate this concept, we investigate another ring resonator that features a larger coupling gap of 605 nm, resulting in an under-coupled resonance mode at 794.13 nm with  $\kappa_e=18.8$  GHz and  $\kappa_{in}=64.8$  GHz (see Supplemental Information Section 5). We burn a spectral hole at the center wavelength of this resonance mode using a burning power of 100 nW. Figure 5C shows the transmission and absorption (inset) spectra of the device after the hole burning, which features a transmission dip at the center frequency, allowing it to function as a bandstop filter. By fitting the spectrum to a Lorentzian function, we extract the linewidth to be 4.2 MHz and the extinction ratio to be 4.4, with a background transmission of 30%. This smaller extinction ratio compared to the cavity-enhanced bandpass filter is mainly attributed to the challenges in optimizing the spectral hole burning process. While increasing burning power can maximize the extinction ratio for a bandpass filter, achieving optimal condition  $\kappa_e = \kappa_{in}$  for a bandstop filter demands precise control over the burning power to remove a specific amount of ion absorption. However, there is no fundamental limit on the maximum achievable extinction ratio for this bandstop filter, as the optimal condition  $\kappa_e = \kappa_{in}$  gives zero transmission at the burning wavelength, resulting in an infinitely large extinction ratio. Alternatively, we can utilize an even more under-coupled resonance mode that has a larger difference between  $\kappa_e$  and  $\kappa_{in}$  ( $\kappa_e \ll \kappa_{in}$ ) to improve the transmission of the un-burned wavelengths, which would also further increase the extinction ratio.

The response time of the bandstop filter features interesting behavior. As a narrow resonance dip in the under-coupling regime, the bandstop filter induces a negative slope of phase shift, which gives rise to a negative group delay<sup>42</sup>. Therefore, unlike the bandpass filter which delays the input pulse, the bandstop filter advances the pulse in time<sup>41</sup>. Similar to faster than light group velocities, this behavior may seem counter-intuitive because it suggests that the pulse leaves the cavity before it enters<sup>43</sup>. It should be noted, however, that this effect does not violate causality<sup>44</sup>.

To demonstrate negative group delay, we send a weak (5 nW) Gaussian-shaped probe pulse through the filter after a 10  $\mu s$  delay. Figure 5D shows the measured arrival time of the probe pulse transmitted through the bandstop filter (blue), as well as a reference probe pulse (orange). By fitting both pulses with Gaussian functions, we extract the advance of the pulse of the bandstop filter to be  $55 \pm 7$  ns. This measured result is also consistent with the predicted advance time calculated from the hole depth  $d = 1.42$  and linewidth  $\Delta = 4.2$  MHz as  $\Delta t = d/2\pi\Delta = 53$  ns.

Besides demonstrating a bandstop filter at the center of the resonance mode, we also explore the filter behavior when the burning wavelength is detuned from the resonant wavelength. To achieve this, we utilize a CW laser detuned from the resonance wavelength (794.13 nm) by -0.006 nm (794.124 nm) and 0.006 nm (794.136 nm) (Fig. 5B, red arrows). The transmission spectra of the resulting detuned bandstop filters are shown by the blue lines in Fig. 5E and F, respectively.

In contrast to the Lorentzian shape exhibited when the filter aligns with the cavity resonance, the detuned bandstop filters feature Fano-shaped transmission profiles. The detuned filters are symmetric because their burning wavelengths are blue and red-shifted by the same amount with respect to the resonance wavelength. This Fano-shaped distortion is attributed to a dispersion effect originating from the narrow spectral hole burned in the atomic absorption. This dispersion effect induces a frequency-dependent change in the real refractive index component, which subsequently alters the original transmission spectrum<sup>45,46</sup>. By calculating the resulting real refractive index component using the Kramers-Kronig relations based on the absorption spectrum of the ion absorption, we model these Fano-shaped transmissions, as shown in the black line in Fig. 5E, F (see Supplemental Information Section 6), which are in good agreement with the measured data. This model is instrumental for the future implementation of more complicated cavity-enhanced reconfigurable filtering functions, which require a series of bandpass or bandstop filters within a resonance mode<sup>47</sup>.

While the demonstrated bandpass and bandstop filters already feature favorable properties, there is still room for further improvements. We could improve the extinction ratio by more precisely fabricating the gap to precisely match the critical coupling condition. This control would allow us to reduce the minimum transmission below the current value of 1%. Alternatively, we could also get closer to critical coupling by tuning the resonance of the cavity through either gas condensation<sup>48</sup> or electro-optical modulation<sup>38</sup>, or by effectively modulating the coupling gap<sup>49</sup>. We could also improve the extinction ratio by burning a deeper spectral hole. The maximum transmission of the cavity-enhanced filter shown in Fig. 3A is approximately 56%, which means we have a loss of 43%. Our calculation attributes 14% to propagation loss ( $k_p = 2.1 \text{ GHz}$ ), while 29% is due to remaining ion absorption ( $k_{ion} = 4.46 \text{ GHz}$ ) as a result of the imperfect hole burning process (see Supplemental Information Section 7). The propagation loss could be further reduced using a better fabrication techniques<sup>50</sup>, while the remaining ion absorption could be reduced by using a higher burning power or applying a magnetic field<sup>29</sup>. In the case of the bandstop filter, the extinction ratio can also be improved by optimizing the burning power and  $k_e$ .

In conclusion, we demonstrate cavity-enhanced narrowband spectral filters with high extinction ratio using rare-earth-ions doped in thin-film lithium niobate. By controlling the cavity coupling rate, we also show reconfigurable filtering through the creation of a bandstop filter. We note that although the performance of our demonstrated filters surpass those of state-of-the-art ring resonators on the thin-film lithium niobate platform<sup>24–26</sup>, they are not the narrowest when all the visible-wavelength integrated platforms are considered. For example, an ultrahigh-quality factor ring resonator (81 million at  $\sim 1530 \text{ nm}$ ) in  $\text{Si}_3\text{N}_4$ <sup>51</sup> can effectively serve as a bandpass filter with a 4 MHz linewidth, which is narrower than the filters we demonstrate. However, by going to a lower temperature, we could decrease the homogeneous linewidth of the ions and reduce the filter linewidth to as narrow as  $\sim 60 \text{ kHz}$ <sup>39</sup>. Further, by applying a magnetic field, we could create persistent filters<sup>29,39</sup>, which are also promising for quantum information applications<sup>52</sup> and provide additional flexibility to control the wavelength, extinction ratio, linewidth and shape of the filter by adjusting the hole burning process. Note that benefits of using rare-earth-based spectral filters are expected to be more pronounced at shorter wavelengths into the visible range

where several rare-earth transitions exist, since Rayleigh scattering due to sidewall roughness is proportional to  $\lambda^{-4}$ , where  $\lambda$  is the wavelength of light. Future work involves co-integration of electro-optic devices, such as frequency shifters<sup>28,53</sup>, to further broaden the utility of rare-earth spectral tailoring<sup>54</sup>.

## Methods

### Device Fabrication:

We fabricate the devices using 300 nm thick X-cut LN thin films doped with 0.1% Tm<sup>3+</sup> on 2  $\mu\text{m}$  of silicon dioxide on silicon substrates. We use standard electron beam lithography to define patterns in hydrogen silsesquioxane (HSQ) resist with multipass exposure. The patterns are subsequently transferred into the LN thin-film using a commercial inductively coupled plasma reactive ion etching (ICP-RIE) tool. We use Ar<sup>+</sup> plasma to physically etch LN where the plasma power and chamber condition are tuned to minimize surface redeposition of removed LN and other contaminations present in the chamber. After etching, we remove redeposition using RCA SC-1 cleaning procedure. Finally, we anneal the sample at atmospheric pressures in O<sub>2</sub> at 520 °C for two hours, to improve the crystallinity of thin-film lithium niobate.

### Spectral hole burning measurement:

For the spectral hole burning measurements, we generate one burn pulse and two weak probe pulses by modulating a narrowband continuous wave laser (Msquared Solstis) utilizing two fiber-coupled acousto-optic modulators (AOM, Brimrose Corp), which are controlled by an arbitrary waveform generator (Keysight). These two AOMs provide independent control over the power, duration and frequency of the burn and probe pulses. We set the burn pulse duration at a fixed 50  $\mu\text{s}$  and vary its power from 50 nW to 2500 nW for different measurements, while maintaining the probe pulses at a constant 3 nW to avoid affecting the hole population. To probe the transmission of the spectral hole, we slowly sweep the frequency of the probe pulses from -50 MHz to 50 MHz with respect to the burning frequency. The first probe pulse is shortly delayed from the burn pulse by 10  $\mu\text{s}$ , to minimize the spectral hole recovering from excited level population decay. Then we delay another 10  $\text{ms}$  to send the second probe pulse, which is well exceeding the  ${}^3H_4$  and  ${}^3F_4$  lifetimes to ensure complete reset of the burned spectral hole to the original ground level population. We record the probe pulses on a single photon counting module (Excelitas Technologies Inc). The normalization of the first probe pulse to the second allows for the measurement of the transmission spectrum of the spectral hole.

### Slow and fast light measurements:

For the slow and fast light measurement, we use a setup similar to the one used for spectral hole burning measurements, but with one burn pulse and one weak probe pulse. Instead of sweeping the probe frequency, we fix it to match the burn frequency and modulate the probe amplitude into a Gaussian shape. We set the full-width at half maximum of the pulse to 1  $\mu\text{s}$ , yielding a probe bandwidth ( $1/1 \mu\text{s} = 1 \text{ MHz}$ ) much smaller than the created hole. This condition ensures that the probe pulse transmits through the spectral hole without distortion, allowing us to describe the shift in arrival time as  $\Delta t = \pm d/2\pi\Delta$ <sup>37</sup>. To measure the shift in probe pulse arrival time, we generate a reference probe pulse by repeating the same measurement with a much higher burning power of 80  $\mu\text{W}$ , which leads to a very broad spectral hole (>1 GHz) causing

negligible changes in the group velocity. The resulting reference probe pulse is therefore considered unshifted in arrival time and serves as a benchmark for evaluating the time delay or advance.

## Acknowledgements

The authors would like to acknowledge support from the National Science Foundation (Grant No. OMA2137723). The Waks group would also like to acknowledge financial support from the National Science Foundation (Grant No. OMA1936314), the U.S. Department of Defense contract (Grant No. H98230-19-D-003/008), and the Maryland-ARL Quantum Partnership (Grant No. W911NF1920181). The Lončar group would also like to acknowledge financial support from the National Science Foundation (Grant No. EEC1941583) and the Army Research Office MURI (Grant No. W911NF1810432).

## Author contributions

Y.Z. and N.S. conceived the experiment. D.R. fabricated the device. Y.Z. performed the experiment. D.F. and S.D. supported in setting up the experiment. Y.Z. analyzed the data. Y.Z., E.W. and N.S. prepared the manuscript and all authors reviewed it and discussed the results. E.W. and M.L. supervised the experiment.

## References

1. Feldmann, J. *et al.* Parallel convolutional processing using an integrated photonic tensor core. *Nature* **589**, 52–58 (2021).
2. Yang, Z., Albrow-Owen, T., Cai, W. & Hasan, T. Miniaturization of optical spectrometers. *Science (80-. )*. **371**, (2021).
3. Dandin, M., Abshire, P. & Smela, E. Optical filtering technologies for integrated fluorescence sensors. *Lab Chip* **7**, 955–977 (2007).
4. Feng, H. *et al.* Integrated lithium niobate microwave photonic processing engine. 1–25
5. Frank, I. W., Zhang, Y. & Loncar, M. Nearly arbitrary on-chip optical filters for ultrafast pulse shaping. *Opt. Express* **22**, 22403 (2014).
6. Weiner, A. M. Ultrafast optical pulse shaping: A tutorial review. *Opt. Commun.* **284**, 3669–3692 (2011).
7. Harris, T. L. *et al.* Multigigahertz range-Doppler correlative signal processing in optical memory crystals. *Appl. Opt.* **45**, 343–352 (2006).
8. Yoo, S. J. B. for WDM Network Applications. *J. Light. Technol.* **14**, 955–966 (1996).
9. Thiel, C. W., Böttger, T. & Cone, R. L. Rare-earth-doped materials for applications in quantum information storage and signal processing. *J. Lumin.* **131**, 353–361 (2011).
10. Böttger, T., Thiel, C. W., Cone, R. L. & Sun, Y. Effects of magnetic field orientation on optical decoherence in Er<sup>3+</sup>: Y<sub>2</sub>SiO<sub>5</sub>. *Phys. Rev. B - Condens. Matter Mater. Phys.* **79**, 1–8 (2009).
11. Ulrich, L. *et al.* High Rejection and Frequency Agile Optical Filtering of RF Signals Using a Rare Earth Ion-Doped Crystal. *J. Light. Technol.* **40**, 6901–6910 (2022).
12. Beavan, S. E., Goldschmidt, E. A. & Sellars, M. J. Demonstration of a dynamic bandpass



- frequency filter in a rare-earth ion-doped crystal. *J. Opt. Soc. Am. B* **30**, 1173 (2013).
13. Kinos, A., Li, Q., Rippe, L. & Kröll, S. Development and characterization of high suppression and high étendue narrowband spectral filters. *Appl. Opt.* **55**, 10442 (2016).
  14. Zhong, T. *et al.* Nanophotonic rare-earth quantum memory with optically controlled retrieval. *Science (80-. )*. (2017). doi:10.1126/science.aan5959
  15. Liu, C. *et al.* On-demand quantum storage of photonic qubits in an on-chip waveguide. *Phys. Rev. Lett.* **125**, 260504 (2020).
  16. Dutta, S. *et al.* An Atomic Frequency Comb Memory in Rare-Earth-Doped Thin-Film Lithium Niobate. *ACS Photonics* (2022). doi:10.1021/acsp Photonics.2c01835
  17. Raha, M. *et al.* Optical quantum nondemolition measurement of a single rare earth ion qubit. *Nat. Commun.* **11**, 1–6 (2020).
  18. Pak, D. *et al.* Long-range cooperative resonances in rare-earth ion arrays inside photonic resonators. *Commun. Phys.* **5**, 1–8 (2022).
  19. Zhu, D. *et al.* Integrated photonics on thin-film lithium niobate. *Adv. Opt. Photonics* **13**, 242 (2021).
  20. Zhang, M., Wang, C., Kharel, P., Zhu, D. & Lončar, M. Integrated lithium niobate electro-optic modulators: when performance meets scalability. *Optica* **8**, 652 (2021).
  21. Chen, Z. *et al.* Efficient erbium-doped thin-film lithium niobate waveguide amplifiers. *Opt. Lett.* **46**, 1161 (2021).
  22. Luo, Q. *et al.* On-chip erbium-doped lithium niobate waveguide amplifiers [Invited]. *Chinese Opt. Lett.* **19**, 060008 (2021).
  23. Thiel, C. W. *et al.* Optical decoherence and persistent spectral hole burning in Er 3:LiNbO<sub>3</sub>. *J. Lumin.* **130**, 1603–1609 (2010).
  24. Li, Z. *et al.* High density lithium niobate photonic integrated circuits. *Nat. Commun.* **14**, 1–8 (2023).
  25. Hang, M. I. A. N. Z. & Ang, C. H. W. Monolithic ultra-high- Q lithium niobate microring resonator. *Optica* **4**, 1536–1537 (2017).
  26. Desiatov, B., Shams-Ansari, A., Zhang, M., Wang, C. & Lončar, M. Ultra-low-loss integrated visible photonics using thin-film lithium niobate. *Optica* **6**, 380 (2019).
  27. Yang, L., Wang, S., Shen, M., Xie, J. & Tang, H. X. Controlling single rare earth ion emission in an electro-optical nanocavity. *Nat. Commun.* **14**, 1–6 (2023).
  28. Renaud, D. *et al.* Sub-1 Volt and high-bandwidth visible to near-infrared electro-optic modulators. *Nat. Commun.* **14**, 1–7 (2023).
  29. Thiel, C. W., Sun, Y., Bttger, T., Babbitt, W. R. & Cone, R. L. Optical decoherence and persistent spectral hole burning in Tm 3:LiNbO<sub>3</sub>. *J. Lumin.* **130**, 1598–1602 (2010).
  30. Dutta, S., Goldschmidt, E. A., Barik, S., Saha, U. & Waks, E. Integrated Photonic Platform for Rare-Earth Ions in Thin Film Lithium Niobate. *Nano Lett.* **20**, 741–747 (2020).
  31. Lumerical Inc.
  32. Sinclair, N. *et al.* Spectroscopic investigations of a Ti: Tm LiNbO<sub>3</sub> waveguide for photon-echo quantum memory. *J. Lumin.* **130**, 1586–1593 (2010).
  33. Sun, Y., Thiel, C. W. & Cone, R. L. Optical decoherence and energy level structure of 0.1%Tm 3+ :LiNbO 3. *Phys. Rev. B* **85**, 165106 (2012).
  34. Bogaerts, W. *et al.* Silicon microring resonators. *Laser Photonics Rev.* **6**, 47–73 (2012).
  35. McKinnon, W. R. *et al.* Extracting coupling and loss coefficients from a ring resonator.

- Opt. Express* **17**, 18971 (2009).
36. Rabus, D. . Ring Resonators: Theory and Modeling, in Integrated Ring Resonators. *Integr. Ring Reson.* 3–40 (2007).
  37. Buyukkaya, M. A., Lee, C. M., Mansoori, A., Balakrishnan, G. & Waks, E. Low power optical bistability from quantum dots in a nanobeam photonic crystal cavity. *Appl. Phys. Lett.* **121**, (2022).
  38. Xia, K. *et al.* Tunable microcavities coupled to rare-earth quantum emitters. *Optica* **9**, 445 (2022).
  39. Sinclair, N. *et al.* Optical coherence and energy-level properties of a Tm<sup>3+</sup> -doped LiNbO<sub>3</sub> waveguide at subkelvin temperatures. *Phys. Rev. B* **103**, 1–15 (2021).
  40. Maniloff, E. S. *et al.* Power broadening of the spectral hole width in an optically thick sample. *Chem. Phys.* **193**, 173–180 (1995).
  41. Boyd, R. W. Slow and fast light: Fundamentals and applications. *J. Mod. Opt.* **56**, 1908–1915 (2009).
  42. Heebner, J. E. & Boyd, R. W. ‘Slow’ and ‘fast’ light in resonator-coupled waveguides. *J. Mod. Opt.* **49**, 2629–2636 (2002).
  43. Wang, L. J., Kuzmich, A. & Dogariu, A. Gain-assisted superluminal light propagation. *Nature* **406**, 277–279 (2000).
  44. Stenner, M. D., Gauthier, D. J. & Neifeld, M. A. The speed of information in a ‘fast-light’ optical medium. *Nature* **425**, 695–698 (2003).
  45. Taherizadegan, S., Kumar, S., Davidson, J. H., Oblak, D. & Simon, C. The Role of Dispersion in Cavity-Enhanced Atomic Frequency Comb Quantum Memories. QM4C.6 (2023). doi:10.1364/quantum.2023.qm4c.6
  46. Sabooni, M., Li, Q., Rippe, L., Mohan, R. K. & Kröll, S. Spectral engineering of slow light, cavity line narrowing, and pulse compression. *Phys. Rev. Lett.* **111**, 1–5 (2013).
  47. Afzelius, M., Simon, C., De Riedmatten, H. & Gisin, N. Multimode quantum memory based on atomic frequency combs. *Phys. Rev. A - At. Mol. Opt. Phys.* **79**, 1–10 (2009).
  48. Dibos, A. M. *et al.* Purcell Enhancement of Erbium Ions in TiO<sub>2</sub> on Silicon Nanocavities. *Nano Lett.* **22**, 6530–6536 (2022).
  49. Xue, Y. *et al.* Breaking the bandwidth limit of a high-quality-factor ring modulator based on thin-film lithium niobate. *Optica* **9**, 1131 (2022).
  50. Shams-Ansari, A. *et al.* Reduced material loss in thin-film lithium niobate waveguides. *APL Photonics* **7**, (2022).
  51. Spencer, D. T., Bauters, J. F., Heck, M. J. R. & Bowers, J. E. Integrated waveguide coupled Si<sub>3</sub>N<sub>4</sub> resonators in the ultrahigh-Q regime. *Optica* **1**, 153 (2014).
  52. Gündoğan, M., Ledingham, P. M., Kutluer, K., Mazzera, M. & De Riedmatten, H. Solid State Spin-Wave Quantum Memory for Time-Bin Qubits. *Phys. Rev. Lett.* **114**, 1–5 (2015).
  53. Hu, Y. *et al.* On-chip electro-optic frequency shifters and beam splitters. *Nature* **599**, 587–593 (2021).
  54. Saglamyurek, E. *et al.* An integrated processor for photonic quantum states using a broadband light-matter interface. *New J. Phys.* **16**, 0–20 (2014).

## Supplemental Information

### Section 1. Determination of the desired gap distance for the critical coupling condition

We first estimate the ring loss rate based on the selected ring design geometry (1000  $\mu\text{m}$  circumference, 500  $\mu\text{m}$  overlap with c-axis). By calculating the ion absorption at  $\sim 794$  nm in one round trip through the ring waveguide from the product of the ion absorption coefficient (3.5 dB/mm) and the absorbing length (500  $\mu\text{m}$ ), we obtain the amplitude attenuation factor of  $a = 0.82$ , and the ring loss rate of  $\kappa_{in} = 51.0$  GHz (see Eq. (1)(3)).

To determine the desired coupling gap to achieve the critical coupling condition, we apply coupled mode theory<sup>1</sup> to analyze the coupling region of the ring resonator. In the straight coupling region, the evanescent mode coupling between the bus and the ring waveguide results in two new modes, a symmetric and an anti-symmetric mode, as shown in Fig. S1. The electric field amplitude splitting between the waveguides depends sinusoidally on the difference between the effective refractive indices of these modes,  $\Delta n$ , as:  $E_{ring}/E_{bus} = \sin(\frac{\pi\Delta n}{\lambda_0} L_c)$ , where  $L_c = 30$   $\mu\text{m}$  is the coupling region length and  $\lambda_0$  is the free space operating wavelength (794 nm). We simulate  $\Delta n$  as a function of the top gap distance between the bus and ring waveguides, and calculate the resulting ratio between  $E_{ring}$  and  $E_{bus}$ , as shown in Fig. S1 C. The critical coupling condition can be achieved when  $E_{ring}/E_{bus} = \sqrt{1 - a^2} = 0.57$  is satisfied, which corresponds to a gap distance of 510 nm.

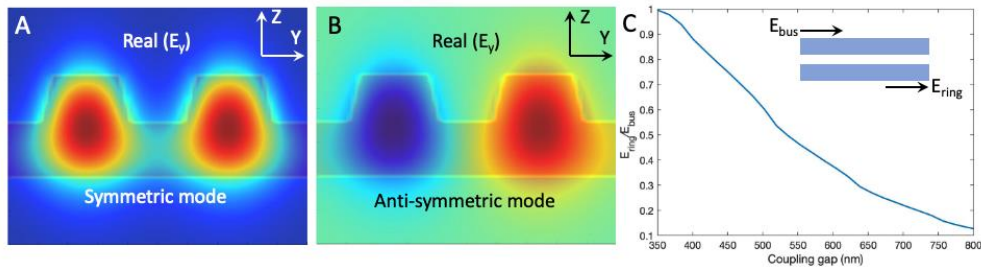


Fig. S1. The  $E_y$  component distribution of the symmetric (A) and anti-symmetric (B) mode in the coupled bus and ring waveguides. (C) The simulated value of  $E_{ring}/E_{bus}$  as a function of the top coupling gap.

### Section 2. Characterization of the propagation loss of ring resonator

We estimate the propagation loss of the ring waveguide by measuring the quality factor of a near-critically coupled bare ring resonator with an identical ring waveguide design, fabricated using the same method on a separate undoped thin-film lithium niobate chip. For this bare ring resonator, we modify the coupling region design for a weaker coupling strength: 5  $\mu\text{m}$  coupling length, 620 nm coupling gap, to match the small ring loss rate contributed from the low propagation loss. Figure S2 shows the transmission spectrum of a near critically-coupled resonance mode of the bare ring resonator (ring length = 878  $\mu\text{m}$ ) at 794.7 nm. We fit the data to a Lorentzian function (see Eq. (1)) and extract the loaded and intrinsic quality factors  $Q_L = 5.42 \times 10^5$  and  $Q_I = 1.1 \times 10^6$ , from which we calculate the propagation loss of 0.7 dB/cm. This

value is also comparable with previous results using the same fabrication methods<sup>2</sup>. This propagation loss could be further reduced by depositing a SiO<sub>2</sub> cladding layer.

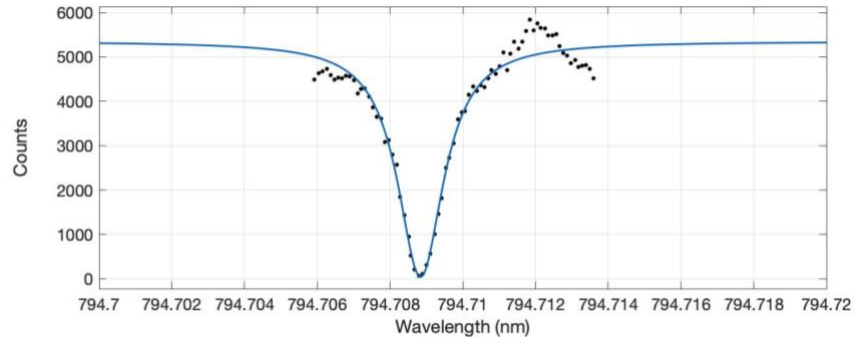


Fig. S2 The transmission spectrum of a near critically-coupled bare ring resonator with identical ring waveguide design fabricated on a separate undoped thin-film lithium niobate chip.

### Section 3. Estimation of the power enhancement in the ring waveguide

The light intensity in the ring waveguide can be much higher than the incident light in the bus waveguide, as the traveling wave in the ring resonator constructively interferes at resonance with the input wave and thus the amplitudes build up. To estimate the intensity enhancement, we consider a simplified model of the ring resonator, as shown in Fig. S3. In the figure, the  $E_{i1}$ ,  $E_{i2}$ ,  $E_{t1}$  and  $E_{t2}$  represent the two input and output ports at the coupling region, with  $r$ ,  $k$  and  $a$  denoting the coupling coefficients and amplitude attenuation factor (same definition as in Eq. (1) of the main text). The intensity enhancement factor is given by<sup>3</sup>:

$$\left| \frac{E_{i2}}{E_{i1}} \right|^2 = \left| \frac{ka}{1 - ar} \right|^2 \quad (S4)$$

When a deep spectral hole is created during the hole burning process, we consider that the ion absorption removed so that  $a \approx 1$ . Meanwhile,  $r$  is extracted to be  $r = 0.83$  from Fig.2(C). For a lossless coupling process, we calculate  $k = 0.56$  using the relation  $r^2 + k^2 = 1$ . With these parameters, we obtain the intensity enhancement in the ring waveguide from Eq.(S1) to be  $\sim 10$ .

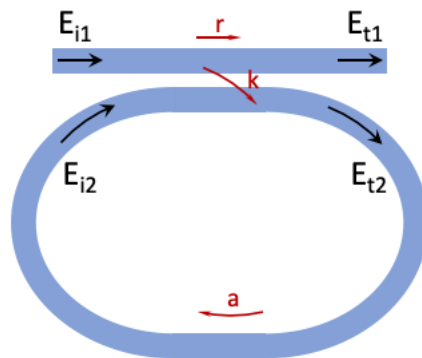


Fig. S3 A simplified model of the ring resonator

## Section 4. Power broadening of spectral hole linewidth

The linewidth of a spectral hole increases with the burning power following a power broadening model<sup>4</sup>:

$$\Gamma_{hole} = \Gamma_L \left[ \left( 1 + \sqrt{1 + (K/\Gamma_L)^2} \right) \times \left( 1 + \sqrt{1 + (K/\Gamma_L)^2 e^{-d}} \right) \right]^{1/2}, \quad (S5)$$

where  $d$  is the initial ion absorption,  $\Gamma_L$  is the fitted homogeneous linewidth that includes linewidth broadening due to laser frequency instability, and  $K^2$  is proportional to the excitation power. We fit the waveguide linewidth data (blue line) in Fig. 3C using Eq. (S2), yielding  $d = 1.10 \pm 0.12$  and  $\Gamma_L = 1.15 \pm 0.21 \text{ MHz}$ . We also compare this extracted homogeneous linewidth with the optical coherence time measured using two-pulse photon echo in the same waveguide at 4K, as shown in Fig. S3. The coherence time is extracted from the exponential decay rate as  $T_2 = 461 \pm 65 \text{ ns}$ , which corresponds to a homogeneous linewidth of  $\Gamma_L = 0.691 \pm 0.113 \text{ MHz}$ . The homogeneous linewidth extracted in both ways are almost consistent. We attribute this shorter coherence time, compared to previous results<sup>5</sup>, to a non-ideal sample-stage thermal contact in the cryostat that we use.

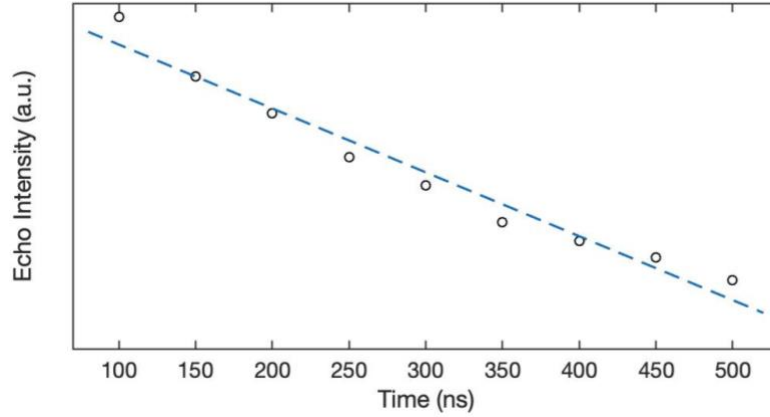


Fig. S4. The echo intensity decays exponentially as a function of delay time in the two-pulse photon echo measurement.

## Section 5. Characterization of the under-coupled resonance mode

To characterize the under-coupled resonance mode at 794.13 nm in ring resonator with a 605 nm coupling gap, we measure the transmission spectrum using an attenuated narrowband tunable laser (Msquared). By scanning the wavelength of the laser, we measure the power of the transmitted light as a function of the wavelength, as shown in Fig. S5. We fit the data to the all-pass ring resonator transmission equation (Eq. (1)) and extract  $r = 0.935$  and  $a = 0.794$ . From this, we calculate  $\kappa_e = 18.8 \text{ GHz}$  and  $\kappa_{in} = 64.8 \text{ GHz}$  using Eq. (2-3).

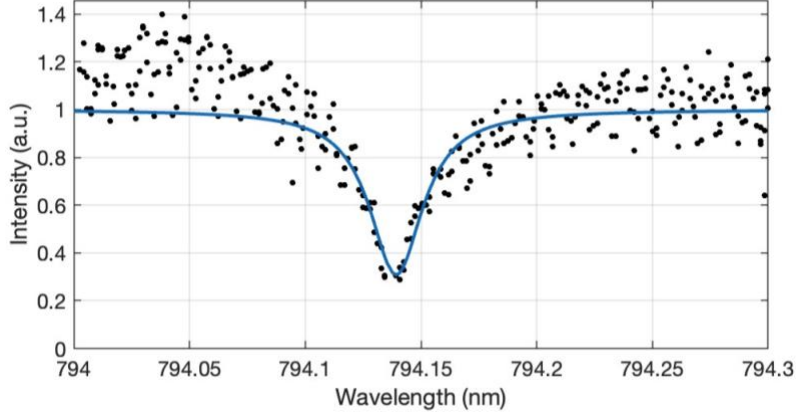


Fig. S5 The transmission spectrum of the under-coupled resonance mode at 794.13 nm

## Section 6. Detuned filter model based on Kramers-Kronig relations

As discussed in Section 5, the transmission spectrum of the under-coupled ring resonator can be described by Eq. (1):

$$T = \frac{r^2 + a^2 - 2ar\cos(\varphi)}{1 + r^2a^2 - 2ar\cos(\varphi)} \quad (S6)$$

where the  $r$  and  $a$  are extracted to be 0.935 and 0.794, and  $\varphi$  is the one-round trip phase given by  $\varphi = n\omega L/c$ , with  $n$  representing the real refractive index of the material. We create a detuned bandstop filter by burning a spectral hole at frequency  $\omega_1$ , detuned by  $\Delta\omega$  from the resonant frequency,  $\omega_0$ . We consider the spectral hole to be Lorentzian-shaped with a hole depth of  $d$  and a linewidth of  $\gamma$ . This spectral hole modifies the near constant ion absorption coefficient  $\alpha_0 = 11.56 \text{ cm}^{-1}$  at 794.13 nm into a frequency-dependent function:

$$\alpha(\omega) = \alpha_0 - \gamma^2 d / [(\omega - \omega_1)^2 + \gamma^2] \quad (S7)$$

From this equation, we can obtain the resulting frequency dependent attenuation factor,  $a(\omega)$ , from absorption coefficient,  $\alpha(\omega)$ , as:

$$a(\omega) = e^{-(\alpha(\omega)L_a + \alpha_p L)/2}, \quad (S8)$$

where  $L_a$  and  $L$  are the effective absorption length (length that overlaps with the c-axis) and the total length in the ring, and  $\alpha_p$  represents the propagation loss characterized in Section 2. Additionally, this narrow spectral hole will also result in a dispersion effect, which will bring in a frequency-dependent change in real refractive index beyond the original constant index  $n_0 = 2.256$ . The complex refractive index can be written as  $\tilde{n}(\omega) = n(\omega) + ik(\omega)$ , where the real part  $n(\omega)$  is responsible for the change in the phase  $\varphi$ , while the imaginary part  $k(\omega)$  is related to the absorption coefficient as:

$$k(\omega) = \alpha(\omega)c/2\omega \quad (S9)$$

The  $n(\omega)$  is connected to  $k(\omega)$  through the Kramers-Kronig relations as:

$$n(\omega) = n_0 + \frac{2}{\pi} \mathcal{P} \int_0^\infty \frac{\omega' k(\omega')}{\omega'^2 - \omega^2} d\omega', \quad (\text{S10})$$

where  $\mathcal{P}$  symbolizes the Cauchy principal value. Utilizing this obtained  $n(\omega)$ , we calculate the phase shift  $\varphi(\omega)$  as:

$$\varphi(\omega) = \frac{\omega}{c} [(L - L_a)n_0 + L_a n(\omega)] = \frac{n_0 \omega L}{c} + \frac{2\omega L_a}{c\pi} \mathcal{P} \int_0^\infty \frac{\omega' k(\omega')}{\omega'^2 - \omega^2} d\omega'. \quad (\text{S11})$$

The first term in Eq. S8 represents the phase caused by the original index  $n_0$ , while the second term denotes the phase resulted from the frequency dependent index change, which only accumulates for an effective length of  $L_a$  that aligns with the ion absorption direction. By substituting Eqs. (S4-8) into Eq. (S3), we fit the measured transmission spectrum of the bandstop filters detuned by  $\pm 0.006 \text{ nm}$  with fitting parameters:  $d = 0.3$ ,  $\gamma = 5 \text{ MHz}$ , as shown in the black curves in Fig. 5E, F of the main text.

### Section 7. Calculation of the loss of the cavity-enhanced bandpass filter

From Fig. 2C of the main text, we extracted the self-coupling rate  $r = 0.83$  and the one-round amplitude transmission,  $a = 0.80$ . However, in the measurement of the cavity-enhanced bandpass filter shown in Fig. 3A, the cavity slightly red shifted from 794.535 nm to 794.65 nm (during the measurement, the burning wavelength is set to be 794.65 nm to keep resonant to the shifted cavity). At this red-shifted wavelength, the ion absorption slightly drops (see Fig. 2B, orange line), resulting in  $a = 0.851$ . Without any hole burning, the transmission is calculated to be 0.51%, by substituting  $r = 0.83$ ,  $a = 0.851$  into Eq. (1). Given the measured spectral hole extinction ratio 110, the center transmission of this bandpass filter is around 56%. Given the measured propagation loss 0.7 dB/cm, we could estimate that within this 43% background loss, 14% is from propagation loss ( $\kappa_p = 2.1 \text{ GHz}$ ) and 29% is from remaining ion absorption, which corresponds to  $\kappa_p = 4.46 \text{ GHz}$ .

### References:

1. Little, B. E. & Huang, W. P. Coupled-Mode Theory for Optical Waveguides. *Prog. Electromagn. Res.* **10**, 217–270 (1995).
2. Desiatov, B., Shams-Ansari, A., Zhang, M., Wang, C. & Lončar, M. Ultra-low-loss integrated visible photonics using thin-film lithium niobate. *Optica* **6**, 380 (2019).
3. Compendium, T. *Integrated Ring Resonators. Integrated Ring Resonators* (2007). doi:10.1007/978-3-540-68788-7
4. Maniloff, E. S. *et al.* Power broadening of the spectral hole width in an optically thick sample. *Chem. Phys.* **193**, 173–180 (1995).
5. Dutta, S. *et al.* An Atomic Frequency Comb Memory in Rare-Earth-Doped Thin-Film Lithium Niobate. *ACS Photonics* (2022). doi:10.1021/acsp Photonics.2c01835